Prominent stress-driven anomalies in superconductivity of yttrium hexahydride

Han Liu,[1,2,*] Chang Liu,[1,2,*,†] Yanming Ma,[1,3,4,‡] and Changfeng Chen[2,§]

[1]*Key Laboratory of Material Simulation Methods and Software of Ministry of Education, College of Physics, Jilin University, Changchun 130012, China*

[2]*Department of Physics and Astronomy, University of Nevada, Las Vegas, Nevada 89154, USA*

[3]*State Key Laboratory of Superhard Materials, College of Physics, Jilin University, Changchun 130012, China*

[4]*International Center of Future Science, Jilin University, Changchun 130012, China*

(Received 6 September 2023; revised 10 December 2023; accepted 5 February 2024; published 20 February 2024)

Yttrium hexahydride is a top superconducting superhydride, but its measured T_c data are widely scattered and well below theoretical predictions. These prominent anomalies remain unresolved despite major efforts, impeding the understanding of this distinct class of superb superconductors. Here, we show that nonhydrostatic stresses, which are omnipresent in high-pressure experiments but omitted in prior theoretical studies, cause large deviations of T_c from hydrostatic values, accounting for the strong scattering of experimental data and, joint with an anharmonic correction, reconciling the diverging theoretical and experimental T_c results. Analysis of stress-induced phonon and charge responses unveils the underlying microscopic mechanisms. These findings offer a viable solution to the notable superconductivity anomalies in YH_6, and the insights have broad implications for other superconducting superhydrides and, more generally, superconductors under extreme compression.

DOI: 10.1103/PhysRevB.109.064513

I. INTRODUCTION

In his seminal work of 1968 [1], Ashcroft raised the intriguing possibility that dense hydrogen could be a high-temperature superconductor, driven by the strong coupling of the conduction electrons in metallized hydrogen to the high-frequency phonons stemming from the light mass of hydrogen atoms. Further theoretical studies proposed that the superconducting critical temperature (T_c) of solid hydrogen could reach hundreds of Kelvins at pressures in the hundreds of gigapascal (GPa) to terapascal range [2–4]. Such extremely high pressures are required to convert hydrogen from the insulating molecular phase to metallic atomic phase, where localized intramolecular bonding charges are driven to participate in itinerant electron conduction. Experimental studies have found [5,6] that the molecular-to-atomic phase transition in hydrogen occurs at pressures above 425–440 GPa, pushing the limit of current experimental synthesis and characterization capabilities. Recent studies [7–9] show that anisotropic stresses promote electronic band gap closure in semiconductors and insulators, reducing hydrogen metallization pressure to a more feasible range of 250–300 GPa [10], opening a fresh avenue for further progress.

Alternatively, Ashcroft later proposed [11] that superconductivity may be realized in hydrogen-rich compounds via chemical precompression to reduce pressure required for reaching the metallic phase. Ensuing theoretical works identified several hydrides, such as CaH_6 [12], H_3S [13,14], YH_6 [15,16], and YH_9 [16], and LaH_{10} [16,17], that host T_c above 200 K at more accessible high pressures. Guided by the computational results, experimental efforts synthesized the predicted compounds with unprecedented high T_c: 203 K in H_3S at 155 GPa [18], 250–260 K in LaH_{10} at 170–190 GPa [19,20], 218–224 K in YH_6 at 165–183 GPa [21–23], 243 K in YH_9 at 201 GPa [21], and 215 K in CaH_6 at 172 GPa [24,25]. These successes spurred tremendous research interest in such superhydrides, and active pursuits continue [26,27]. Meanwhile, it has been noted that measured T_c values of superconducting superhydrides are often strongly scattered and large disparities exist between theoretical and experimental T_c data [21–23]. Among superconducting superhydrides, YH_6 has the most comprehensive results on the pressure-T_c relations from both theory and experiment, revealing that calculated T_c values spread over a wide range 30–50 K above the measured data. It was reported [22] that anharmonic effects can cause a sizable reduction of T_c, but large discrepancies remain, indicating another yet to be identified major mechanism at work.

A crucial missing piece in all previous theoretical works is the effect of nonhydrostatic stresses that are omnipresent in densely compressed samples in diamond anvil cells (DACs). At megabar pressures, severe nonuniform deformations and anisotropic stresses in the vicinity of the sample was revealed by direct x-ray imaging study [28,29] and supported by computational simulations [30]. Such stresses can cause notable structural changes, leading to large variations of other properties, such as T_c in superconducting superhydrides. It is therefore important to elucidate the effects of anisotropic stresses on the structural and superconducting properties of densely compressed superhydrides by establishing the trend and range of property variations and making connection to the experimentally observed anomalous phenomena.

*These authors contributed equally to this work.
†liuchang127@jlu.edu.cn
‡mym@jlu.edu.cn
§changfeng.chen@unlv.edu

In this work, we assess the impact of nonhydrostatic stresses on T_c of superconducting superhydrides via first-principles calculations, focusing on YH_6 for an exemplary case study, where a wealth of data from both theory and experiment allows a systematic comparison and in-depth analysis. Our study reveals sensitive and strong dependence of T_c on the commonly present compressive or shear stresses on YH_6, leading to widely scattered T_c under diverse nonhydrostatic stresses. Notably, the stress modified T_c values are generally lower than the corresponding results under hydrostatic pressures. Combined with the previously obtained anharmonic correction, the present results reconcile the conspicuous disagreement between the theoretical and experimental T_c of YH_6. We analyzed the changes of bonding structure, phonon modes, electronic density of states, and electron-phonon coupling in response to the stresses to probe the mechanisms driving the T_c variations. Our findings show strong effects of nonhydrostatic stresses in modulating T_c of YH_6, and the results have major implications for other high-T_c superconducting superhydrides, which require further investigations from both theory and experiment to establish and elucidate systematic trends. This study also raises a general point that nonhydrostatic stresses may have considerable impact on material properties beyond the standard conceptual understanding and theoretical treatments under hydrostatic pressures, and such effects need to be considered more consistently in high-pressure research.

II. COMPUTATIONAL METHODS

The first-principles total-energy and stress-strain calculations were carried out using the density functional theory as implemented in the Vienna *Ab initio* Simulation Package (VASP) [31,32], adopting the generalized gradient approximation in the framework of the Perdew-Burke-Ernzerhof (PBE) exchange-correlation function [33] and the projector augmented wave approach [34] to describe electron-ion interaction. The $1s^1$ and $4s^2 4p^6 4d^1 5s^2$ valence electron configurations were used for hydrogen and yttrium, respectively. The plane wave basis set is constructed with an energy cutoff of 700 eV and the Brillouin zone is sampled in the Monkhorst-Pack scheme [35] with a k-point resolution of $2\pi \times 0.03$ Å^{-1}, achieving an energy convergence around 1 meV per atom. To determine the stress responses, we employed a computational approach that has been extensively used in determining the stress-strain relations in diverse materials under various loading conditions [36–44]. At each step of the constrained structural optimization, both the shape of the deformed unit cell and the atomic relaxation are fully determined. To ensure a quasistatic strain path, the starting position for each strain step is taken from the relaxed coordinates of the previous strain step. At each step, the selected shear or compressive stress was fixed while simultaneously relaxing all atomic positions and the other independent components of the strain tensors to ensure that the residual forces and stress deviations were less than 0.005 eV/Å and 0.1 GPa, respectively.

Electron-phonon coupling (EPC) calculations were performed using the QUANTUM ESPRESSO (QE) code [45] within the framework of the density-functional perturbation theory (DFPT) [46], employing the plane-wave pseudopotential method and PBE exchange-correlation functional. Superconductivity was studied in the framework of conventional phonon-mediated Bardeen-Copper-Schrieffer [47,48] and Migdal-Eliashberg [49,50] theory. For calculations involving the primitive cell YH_6 structure under hydrostatic pressure, we used an energy cutoff of 80 Ry and a $24 \times 24 \times 24$ k mesh in the PAW-PBE framework, along with an $8 \times 8 \times 8$ q mesh for the phonon calculations, producing T_c values converged to within 5 K at a Gaussian smearing width of 0.03 Ry. When the YH_6 crystal is deformed under strains, its symmetry is reduced, resulting in a higher number of irreducible k and q points, requiring a smaller number of total such points to reach the same level of accuracy. Accordingly, different k mesh and q mesh were used for T_c calculations that produce similarly converged T_c. For instance, at the compressive strain of $\epsilon_{zz} = 0.02$ in the [011] direction at 165 GPa, a $12 \times 12 \times 12$ k mesh and a $4 \times 4 \times 4$ q mesh were used, while under a compressive strain of $\epsilon_{zz} = 0.06$ in the [111] direction at 165 GPa, a $16 \times 16 \times 16$ k mesh and a $4 \times 4 \times 4$ q mesh were used, resulting in T_c convergence around 5 K in all the cases. More details on the k-mesh and q-mesh convergence tests are presented in Supplemental Material (see Fig. S1 and Table S1) [51].

III. RESULTS AND DISCUSSION

A. Stress-strain relations in compressed YH_6

To evaluate stress-induced property changes in YH_6, we first examine its stress responses to a variety of anisotropic strains over a range of hydrostatic pressures corresponding to those reported in recent experimental synthesis and characterization studies. Our objective here is to determine the range of elastic and dynamic stability of the YH_6 crystal under various loading conditions and set the maximal strains that can be sustained by the deformed crystal. To this end, we employed a first-principles method to assess stress-strain relations [36–44] and obtained results under compression and shear strains at the hydrostatic pressures of 165 GPa, 200 GPa, and 240 GPa, where ample experimental T_c data and theoretical results calculated under hydrostatic pressures are available to allow a systematic analysis. Calculated stress-strain relations shown in Fig. 1 indicate that YH_6 crystal can sustain anisotropic stresses up to 45 GPa under 5–6 % compressive strains and up to 30 GPa under 8–12 % shear strains, and the maximal nonhydrostatic stresses generally rise with increasing hydrostatic pressures. These findings show that YH_6 can sustain substantial deformations under diverse nonhydrostatic stresses, which are commonly present in DAC compression experiments reaching megabar pressures. It is noted that in ultra-high-pressure experiments, the synthesized samples are very small in size and often polycrystal and multiphase in nature, making it hard to clearly identify the strain state in the specimen, which is further complicated by the sensitivity and variation in each loading. Therefore, in this study, we do not attempt to match the calculated results to specific measured data; instead, we establish the strains generated along various loading paths, and the obtained results provide the corresponding ranges of property changes within the strains that can be sustained by the YH_6 crystal structure.

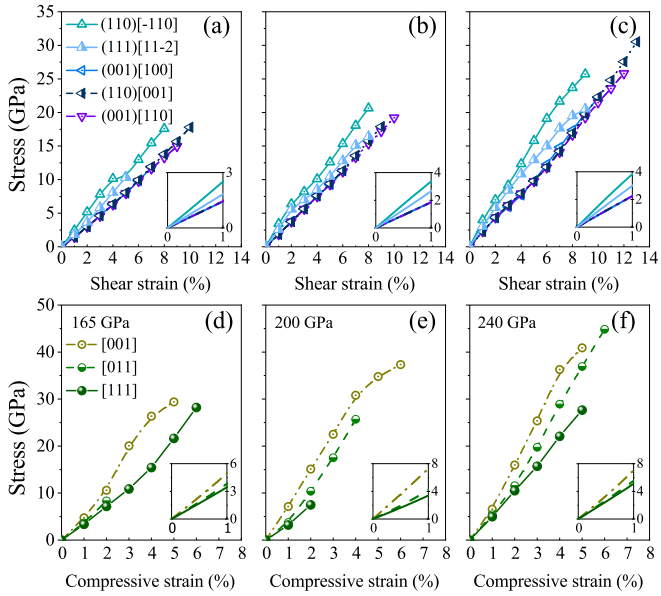

FIG. 1. Stress responses of YH_6 to various (a)–(c) shear and (d)–(f) compressive strains at hydrostatic pressures of (a), (d) 165 GPa, (b), (e) 200 GPa and (c), (f) 240 GPa. The stresses are calculated up to the highest strains under which the deformed crystal remains dynamically stable. The inset in each panel shows the stress responses up to 1% strain, which measure the elastic moduli along various deformation paths, some of which are nearly degenerate, especially under shear strains.

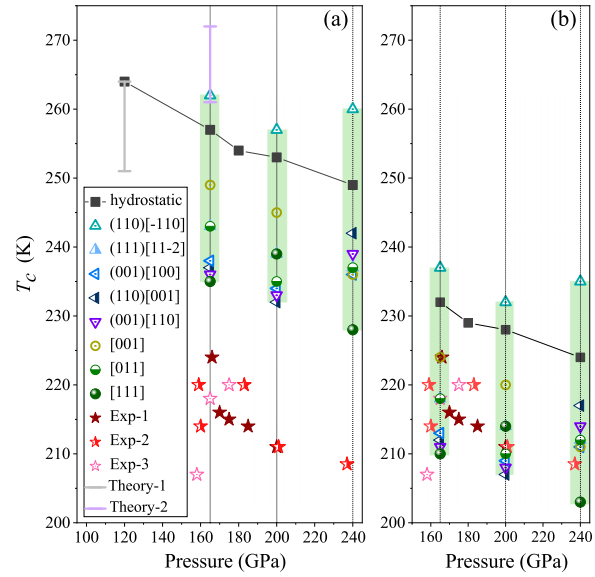

FIG. 2. (a) Calculated T_c of YH_6 at selected hydrostatic pressures (black squares) and under nonhydrostatic stresses (triangles and circles; same symbols for the shear and compressive stresses as in Fig. 1) at 165, 200, and 240 GPa, compared with available experimental data, Expt-1 [22], Expt-2 [21] and Expt-3 [23], and with previously calculated T_c of YH_6 at hydrostatic pressures, Theory-1 [15] and Theory-2 [22]. (b) Same T_c data, but with the theoretical results rigidly downshifted by 25 K as an approximate account for the T_c reduction caused by anharmonic effects [22].

B. Stress-driven variations of superconducting T_c in compressed YH_6

Following the calculations of stress-strain relations, we evaluated T_c of YH_6 under nonhydrostatic stresses superimposed on hydrostatic pressures along various structural deformation paths. The electron-electron interaction is accounted for by the Coulomb pseudopotential μ^* that is often treated as an empirical parameter at in the range 0.10–0.13 in most previous studies. For YH_6, first-principles calculations obtained $\mu^* = 0.11$ [52], which is adopted in this work. Our calculated T_c data under hydrostatic pressures are in agreement with previously reported results [15,16,22] and, importantly, follow the descending trend with rising pressure as seen in experimentally measured data [21–23], but the values are significantly (30–50 K) above the scattered experimental results. To assess the impact by nonhydrostatic stresses, we examined T_c at the maximal strains under which the crystal remains dynamically stable along each deformation path, and the results establish the range of possible T_c variations under the examined strains. We also studied T_c changes along selected deformation paths to evaluate strain dependence of T_c. We summarize in Fig. 2(a) the theoretical T_c values at the maximal strains on all the examined strain paths, along with a comparison with available experimental data over a wide range of pressures. It is seen that nonhydrostatic stresses cause substantial (25–32 K) changes in T_c, mostly large downshifts from the hydrostatic values across the selected pressures. The obtained T_c data are still notably higher than the experimental values. A recent study showed that the anharmonic effects in YH_6 produced a correction of 25 K downshift in T_c at 165 GPa [22], but that correction alone was unable to explain the consistently larger discrepancies between the theoretical and experimental T_c of YH_6 [22]. Currently, no rigorous theoretical treatment is available for the joint anharmonic and nonhydrostatic effects. So we chose to account for the joint effects via a rigid downshift of our calculated T_c by 25 K, assuming that the anharmonic correction is uniformly applied to all the theoretical data. Results in Fig. 2(b) show that such corrected theoretical data overlap with the experimental data, suggesting that the present approach likely captures the main physics of superconducting properties of YH_6 governed by the anharmonic and nonhydrostatic stress effects, although further studies are required to develop a more comprehensive theoretical treatment.

It is known that the strain states in DAC compressed specimens under ultrahigh pressures in the megabar regime are highly sensitive to loading conditions [10]. Consequently, experimental results from different runs that use different pressure cells are expected to harbor more distinct stress states and, as a result, exhibit more pronounced scattering in the measured data. In the reported experimental results on YH_6, separate experimental measurements by different research groups were performed around the pressure range of 160–170 GPa, where the maximal T_c is located and thus attracted the most research interest. The T_c data obtained from the different experimental runs by different research groups likely host distinct stress states, leading to the observed scattering of the measured T_c data. At higher pressures, there are fewer experimental data and, in particular, in the pressure range of 205–240 GPa only one set of experimental data was

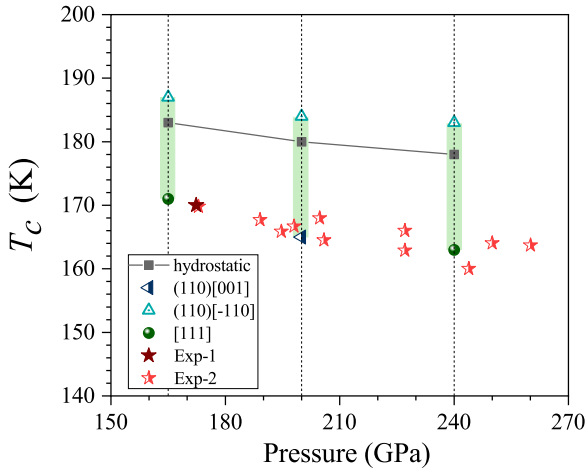

FIG. 3. Calculated T_c of YD_6 at selected hydrostatic pressures (black squares) and under nonhydrostatic stresses (triangles and circles; same symbols for the shear and compressive stresses as in Fig. 1) at 165, 200, and 240 GPa, compared with available experimental data, Expt-1 [22] and Expt-2 [21].

reported, and these data were obtained from the same experimental run using the same press cell, which is expected to host consistent stress states under changing pressure. Therefore, there is a lack of scattering in the measured data at higher pressures, which likely stems from an insufficient amount of experimental data from different experimental runs. This result is not in any contradiction with our theoretical results that predict that different stress states would produce data scattering, but consistent stress states would not generate such data scattering.

Due to the larger atomic mass of deuterium (D) compared to hydrogen (H), the anharmonicity in YD_6 is expected to be notably smaller than in YH_6. We thus performed calculations on YD_6 to help mitigate uncertainties arising from the anharmonic corrections and provide a clearer view on the nonhydrostatic strain effect on T_c. At each hydrostatic pressure, we selected the strained structures with the highest and lowest T_c values in YH_6, as well as the structure at equilibrium, for additional calculations of the corresponding superconducting properties in YD_6. This approach allows us to profile the T_c range in strained YD_6. The results, shown in Fig. 3, reveal that the calculated T_c data of YD_6 under hydrostatic pressures are higher than the experimental data, but with considerably reduced differences compared to the results for YH_6 as seen in Fig. 2. When nonhydrostatic stresses are considered, the calculated T_c reach the same level of agreement with the experimentally measured data without the uniform downward shift as in the case of YH_6. These results help clarify and verify the significant effect of nonhydrostatic stresses on superconductivity of YH_6.

From Fig. 2(b) it is noted that the experimentally measured T_c data scatter in the lower range of the theoretically predicted values. An examination of the stress-strain relations in Fig. 1 reveals that these lower calculated T_c values all occur on the deformation paths that exhibit lower rates of stress increase with rising strain. In other words, these paths exhibit relatively lower elastic moduli, which measure the ability of the crystal to resist the corresponding structural deformations. As a result, the lower T_c values on the lower-moduli deformation paths are more likely to occur in the nonhydrostatic stress environments in DAC compression experiments, which explains the observation that only the lower-range values of theoretically predicted T_c overlap with the experimental data. It should be pointed out, however, based on the calculated results, higher T_c, including those above the hydrostatic values, may occur if the crystal is deformed along strain paths hosting such higher T_c, e.g., along the (110)[−110] shear direction. Such deformation paths with higher elastic moduli may be realized under certain loading conditions or promoted by microstructural textures of the sample, thereby generating considerably higher T_c under suitable strain conditions.

The stress-strain relations in Fig. 1 also show that multiple deformation paths under shear or compressive strains exhibit similarly slow-rising responding stresses with low elastic moduli, which suggests that these deformation modes are likely to coexist in different parts of the sample in the inhomogeneous loading environments commonly occurring under DAC compression. Meanwhile, results in Fig. 2 reveal that these low-moduli paths host nearly identical T_c values. These results indicate that despite the possibly varied deformation modes, the resulting T_c will be nearly uniform throughout the sample. This analysis also applies to polycrystalline samples that contain different domains, which are expected to sustain different strain conditions but still host similar T_c values.

We have performed further calculations to explore whether biaxial strains combining compression and shear deformation modes would cause further reduction in T_c compared with the results under uniaxial compression or shear strains. Since the [111] compression leads to the most significant T_c decrease at 165 GPa and 240 GPa (see Fig. 2), we chose the deformed structure under large [111] compressive strains approaching the dynamic stability limit to experience additional shear strains to look for possible further T_c decrease under the biaxial strains. Similarly, at 200 GPa, the (110)[001] and (001)[110] shear deformed structures exhibit the most T_c reduction from the hydrostatic values approaching the dynamic stability limits (see Fig. 2), and we chose these deformed structures to experience additional compressive strains. On each of the selected biaxial deformation path, the superconducting properties of the maximally strained structure with dynamic stability are obtained (see Table S2 in Supplemental Material [51]). Compared with the calculated T_c results under uniaxial strains, results under biaxial strains mostly show less decrease in T_c, with only the result under biaxial strain combining [111] compression and [11-2] shear along the (111) crystalline plane showing a slight further decrease in T_c. In general, lattice vibrations exhibit a clear and consistent tendency to soften more significantly with increasing strains, but $N(E_F)$ does not follow a clearly regulated variation pattern under strains. Our results indicate that biaxial strains have no clear advantage in reducing T_c from the hydrostatic values when the structure is deformed to the dynamic stability limits under combined compression and shear deformation modes compared to the results obtained under the uniaxial strains that deform crystal to the dynamic stability limits along distinct deformation paths.

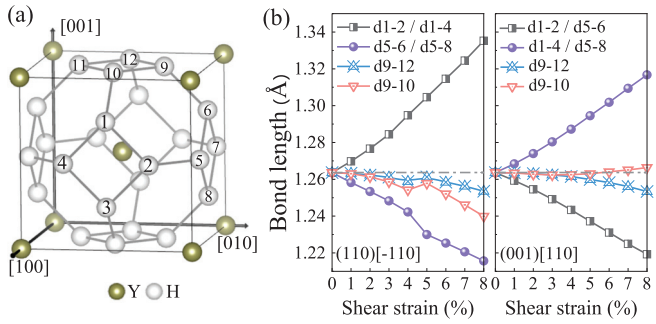

FIG. 4. (a) Crystal structure of YH_6 in Im-3m symmetry, with Y atoms (gold spheres) and square units of H atoms (gray spheres) occupying body-centered cubic lattice sites, forming a sodalite-like cage network. (b) Variation of bond lengths under the (110)[−110] or (001)[110] shear strains. The H-H bonds, which have the same length under hydrostatic pressures, deform differently under nonhydrostatic stresses, resulting in several distinct bond lengths. Each H-H bond shown here has three additional symmetry related equivalent bonds in the examined shear deformed structures.

C. Mechanisms for the anomalies in superconductivity of compressed YH_6

To elucidate the mechanisms driving the T_c variations under nonhydrostatic stresses, we examine the stress-induced structural changes in YH_6, then correlate such changes with the variations of the electronic and phonon properties. Here, we take the exemplary cases of (110)[−110] and (001)[110] shear strains at 165 GPa for an in-depth analysis. The stress-strain relations in Fig. 1 show that these two cases have the highest and lowest elastic moduli, respectively, among the examined shear deformation paths, and the latter is essentially degenerate with other two shear strain paths. Figure 4 shows the variations of bond lengths in deformed YH_6 crystal, which reveal notably stronger deviations from the hydrostatic values under the higher-modulus (110)[−110] strain path compared to that under the lower-modulus (001)[110] shear strain path. Such contrasting structural changes are expected to produce distinct property responses.

We first compare the calculated phonon dispersions of YH_6 along these two shear deformation paths (Fig. 5), revealing that deformation-induced phonon mode softening occurs in both cases, but is much more pronounced along the (110)[−110] shear path than along the (001)[110] path, due to the more stretched thus weakened bonds in the former (Fig. 4). In particular, under large (110)[−110] strains, the lowest optical phonon branch undergoes especially pronounced softening, making a significant contribution to the enhancement of the electron-phonon coupling parameter λ, which is further augmented by the contributions from the notably softened acoustic phonon modes. Meanwhile, under the (001)[110] shear strains, both the acoustic and low-frequency optical phonon modes are softened to a lesser extent and, moreover, accompanied by more notable reductions of the spectral weights compared to the undeformed case. Consequently, the resulting α^2F and λ are little changed in the strained crystal. This trend of stronger electron-phonon coupling enhancement on more deformed high-modulus strain paths also holds for other shear and compressive strain paths across all examined pressures, as shown by the computed results shown in Table I and Figs. S2– S6 [51].

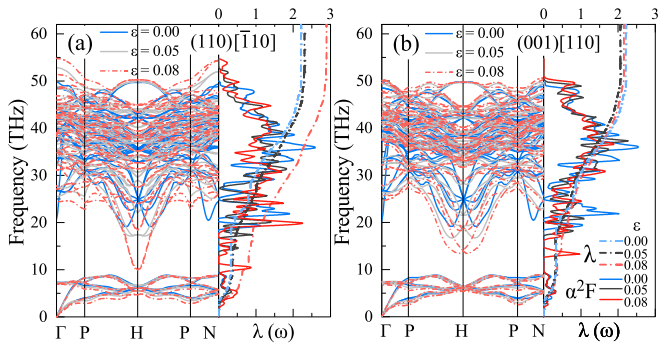

FIG. 5. Phonon dispersion curves under (a) the (110)[−110] and (b) the (001)[110] shear strains at $\epsilon = 0.00$, 0.05 and 0.08 (left panels), along with the Eliashberg spectral function $\alpha^2F(\omega)$ and electron-phonon coupling parameter λ (right panels) at 165 GPa.

Besides the distinct phonon modes, there are also contrasting changes in the electronic density of states at the Fermi energy, $N(E_F)$, under the high- and low-modulus deformations, due to band shifts occurring on different strain paths. Under the (110)[−110] strain, $N(E_F)$ is notably higher, rising above the value for the undeformed crystal, than the value under the (001)[110] strain. Similarly lower values are also found consistently on other low-modulus shear strain paths at 165 PGa and at higher pressures of 200 GPa and 240 GPa, and this pattern of higher $N(E_F)$ on strain paths with higher elastic modulus also holds under the compressive strains across the examined pressures, although the highest $N(E_F)$ is still lower than that of the undeformed crystal (see data in Table I). The stress-induced bonding and electronic variations produce systematic changes in λ and $N(E_F)$, which, in turn, generate different T_c. The phonon frequency $\omega_{\log}$ also plays a role in differentiate T_c values when other factors are closely matched (see data in Table I).

Under stress, various bonds in the crystal experience nonuniform variations, changing the bonding interaction and reducing the lattice symmetry. These changes cause shifts of the electronic bands, leading to variations in the density of states at the Fermi level, $N(E_F)$. The dependence of the electronic band structure on the bonding structure and bond length changes is quite complex, which dictate that there is no simply systematic pattern for $N(E_F)$ variations. Instead, the results depend on the stress states under various deformation modes, and must be determined for specific cases under study, as obtained in our calculations.

IV. CONCLUSIONS

In this work, we have demonstrated via first-principles calculations that nonhydrostatic stresses can cause significant T_c variations in superconducting superhydride YH_6 over a large range of experimentally explored high pressures. The resulting T_c values scatter widely and mostly trend lower than the corresponding value at hydrostatic pressure. These results explain the wide scattering of experimental T_c data, which are driven by distinct stress states in the DAC sample

TABLE I. Computed $N(E_F)$ (states/(spin · Ry · cell), $\omega_{\log}$ (K), λ, and T_c (K) for YH_6 at various shear and compressive strains.

	165 GPa					200 GPa					240 GPa				
	Strain	$N(E_F)$	$\omega_{\log}$	λ	T_c	Strain	$N(E_F)$	$\omega_{\log}$	λ	T_c	Strain	$N(E_F)$	$\omega_{\log}$	λ	T_c
hydrostatic	0.00	9.40	1167	2.21	257	0.00	9.20	1262	1.97	253	0.00	9.00	1323	1.83	249
(001)[110]	0.09	8.70	997	2.26	236	0.10	8.59	1052	2.05	233	0.12	8.69	810	2.31	239
(110)[001]	0.10	8.66	896	2.45	237	0.09	8.56	1139	1.94	232	0.13	8.73	882	2.30	242
(001)[100]	0.07	8.78	1075	2.17	238	0.06	8.41	1229	1.87	234	0.10	8.66	901	2.20	236
(111)[11$\bar{2}$]	0.05	8.95	1127	2.17	243	0.08	8.67	1173	1.98	239	0.09	8.62	455	3.01	238
(110)[$\bar{1}$10]	0.08	9.54	873	2.89	262	0.08	9.33	1043	2.34	257	0.09	9.31	656	2.85	260
[111]	0.06	8.61	1056	2.12	235	0.02	8.74	1283	1.85	239	0.05	8.35	1248	1.74	228
[011]	0.02	8.85	1175	2.08	243	0.04	8.59	1252	1.84	235	0.06	8.57	1191	1.87	237
[001]	0.05	9.14	1046	2.34	249	0.06	8.97	1125	2.08	245	0.05	8.72	1257	1.78	236

chamber on divergent loading paths on different experimental runs. Moreover, after accounting for an anharmonic correction, the present results provide a viable solution to the large discrepancies between theoretical and experimental T_c that persist over the entire explored pressure range. An analysis of stress-induced phonon and electronic responses elucidates the mechanisms stemming from the bond-length changes that impact the lattice dynamics and phonon modes and the electronic band shifts, which combine to produce the large T_c anomalies in YH_6.

The present study goes beyond the standard paradigm of material physics at hydrostatic pressures, opening a new avenue for probing superconducting superhydrides under rich and diverse stress conditions. The resulting expanded realm of anisotropic stress environments raises fresh challenges and opportunities. For instance, an integrated description of anharmonic and nonhydrostatic effects requires further computational advances, and the outcome should help improve the understanding of pertinent physical processes and properties. Moreover, recent studies [53,54] showed that hydrogen vacancies in substoichiometric superhydrides and thermally excited hydrogen sublattice diffusion have notable effects on the behaviors of superhydrides. An in-depth study of these thermal effects under nonhydrostatic stresses may reveal interesting new phenomena, which could lead to a deeper understanding of this class of high-T_c superconductors. The resulting insights may help elucidate properties of a broad variety of materials at ultrahigh pressures where nonhydrostatic stresses are often present.

ACKNOWLEDGMENTS

This work was supported by National Key Research and Development Program of China (Grant No. 2022YFA1402304) and Natural Science Foundation of China (Grant No. 12202158).

[1] N. W. Ashcroft, Metallic hydrogen: A high-temperature superconductor?, Phys. Rev. Lett. **21**, 1748 (1968).
[2] L. Zhang, Y. Niu, Q. Li, T. Cui, Y. Wang, Y. Ma, Z. He, and G. Zou, Ab initio prediction of superconductivity in molecular metallic hydrogen under high pressure, Solid State Commun. **141**, 610 (2007).
[3] P. Cudazzo, G. Profeta, A. Sanna, A. Floris, A. Continenza, S. Massidda, and E. K. U. Gross, Ab initio description of high-temperature superconductivity in dense molecular hydrogen, Phys. Rev. Lett. **100**, 257001 (2008).
[4] J. M. McMahon and D. M. Ceperley, High-temperature superconductivity in atomic metallic hydrogen, Phys. Rev. B **84**, 144515 (2011).
[5] P. Loubeyre, F. Occelli, and P. Dumas, Synchrotron infrared spectroscopic evidence of the probable transition to metal hydrogen, Nature (London) **577**, 631 (2020).
[6] M. I. Eremets, A. P. Drozdov, P. P. Kong, and H. Wang, Semimetallic molecular hydrogen at pressure above 350 GPa, Nature Phys. **15**, 1246 (2019).
[7] C. Liu, X. Song, Q. Li, Y. Ma, and C. Chen, Smooth flow in diamond: Atomistic ductility and electronic conductivity, Phys. Rev. Lett. **123**, 195504 (2019).
[8] C. Liu, X. Song, Q. Li, Y. Ma, and C. Chen, Superconductivity in compression-shear deformed diamond, Phys. Rev. Lett. **124**, 147001 (2020).
[9] C. Liu, X. Song, Q. Li, Y. Ma, and C. Chen, Superconductivity in shear strained semiconductors, Chin. Phys. Lett. **38**, 086301 (2021).
[10] X. Song, C. Liu, Q. Li, R. J. Hemley, Y. Ma, and C. Chen, Stress-induced high-T_c superconductivity in solid molecular hydrogen, Proc. Natl. Acad. Sci. USA **119**, e2122691119 (2022).
[11] N. W. Ashcroft, Hydrogen dominant metallic alloys: high temperature superconductors?, Phys. Rev. Lett. **92**, 187002 (2004).
[12] H. Wang, J. S. Tse, K. Tanaka, T. Iitaka, and Y. Ma, Superconductive sodalite-like clathrate calcium hydride at high pressures, Proc. Natl. Acad. Sci. USA **109**, 6463 (2012).
[13] Y. Li, J. Hao, H. Liu, Y. Li, and Y. Ma, The metallization and superconductivity of dense hydrogen sulfide, J. Chem. Phys. **140**, 174712 (2014).
[14] D. Duan, Y. Liu, F. Tian, D. Li, X. Huang, Z. Zhao, H. Yu, B. Liu, W. Tian, and T. Cui, Pressure-induced metallization of dense $(H_2S)_2H_2$ with high-Tc superconductivity, Sci. Rep. **4**, 6968 (2014).

[15] Y. Li, J. Hao, H. Liu, J. S. Tse, Y. Wang, and Y. M. Ma, Pressure-stabilized superconductive yttrium hydrides, Sci. Rep. **5**, 9948 (2015).

[16] F. Peng, Y. Sun, C. J. Pickard, R. J. Needs, Q. Wu, and Y. Ma, Hydrogen clathrate structures in rare earth hydrides at high pressures: Possible route to room-temperature superconductivity, Phys. Rev. Lett. **119**, 107001 (2017).

[17] H. Liu, I. I. Naumov, R. Hoffmann, N. W. Ashcroft, and R. J. Hemley, Potential high-T-c superconducting lanthanum and yttrium hydrides at high pressure, Proc. Natl. Acad. Sci. USA **114**, 6990 (2017).

[18] A. P. Drozdov, M. I. Eremets, I. A. Troyan, V. Ksenofontov, and S. I. Shylin, Conventional superconductivity at 203 kelvin at high pressures in the sulfur hydride system, Nature (London) **525**, 73 (2015).

[19] M. Somayazulu, M. Ahart, A. K. Mishra, Z. M. Geballe, M. Baldini, Y. Meng, V. V. Struzhkin, and R. J. Hemley, Evidence for superconductivity above 260 K in lanthanum superhydride at megabar pressures, Phys. Rev. Lett. **122**, 027001 (2019).

[20] A. P. Drozdov, P. P. Kong, V. S. Minkov, S. P. Besedin, M. A. Kuzovnikov, S. Mozaffari, L. Balicas, F. F. Balakirev, D. E. Graf, V. B. Prakapenka, E. Greenberg, D. A. Knyazev1, M. Tkacz, and M. I. Eremets, Superconductivity at 250 K in lanthanum hydride under high pressures, Nature (London) **569**, 528 (2019).

[21] P. Kong, V. S. Minkov, M. A. Kuzovnikov, A. P. Drozdov, S. P. Besedin, S. Mozaffari, L. Balicas, F. F. Balakirev, V. B. Prakapenka, S. Chariton, D. A. Knyazev, E. Greenber, and M. I. Eremets, Superconductivity up to 243 K in the yttriumhydrogen system under high pressure, Nature Commun. **12**, 5075 (2021).

[22] I. A. Troyan, D. V. Semenok, A. G. Kvashnin, A. V. Sadakov, O. A. Sobolevskiy, V. M. Pudalov, A. G. Ivanova, V. B. rakapenka, E. Greenberg, A. G. Gavriliuk, I. S. Lyubutin, V. V. Struzhkin, A. Bergara, I. Errea, R. Bianco, M. Calandra, F. Mauri, L. Monacelli, R. Akashi, and A. R. Oganov, Anomalous high-temperature superconductivity in YH_6, Adv. Mater. **33**, 2006832 (2021).

[23] Y. Wang, K. Wang, Y. Sun, L. Ma, Y. Wang, B. Zou, G. Liu, M. Zhou, and H. Wang, Synthesis and superconductivity in yttrium superhydrides under high pressure, Chin. Phys. B **31**, 106201 (2022).

[24] L. Ma, K. Wang, Y. Xie, X. Yang, Y. Wang, M. Zhou, H. Liu, X. Yu, Y. Zhao, H. Wang, G. Liu, and Y. Ma, High-temperature superconducting phase in clathrate calcium hydride CaH_6 up to 215 K at a pressure of 172 GPa, Phys. Rev. Lett. **128**, 167001 (2022).

[25] Z. Li, X. He, C. Zhang, X. Wang, S. Zhang, Y. Jia, S. Feng, K. Lu, J. Zhao, J. Zhang, B. Min, Y. Long, R. Yu, L. Wang, M. Ye, Z. Zhang, V. Prakapenka, S. Chariton, P. A. Ginsberg, J. Bass *et al.*, Superconductivity above 200 K discovered in superhydrides of calcium, Nature Commun. **13**, 2863 (2022).

[26] X. Zhong, Y. Sun, T. Iitaka, M. Xu, H. Liu, R. J. Hemley, C. Chen, and Y. Ma, Prediction of above-room-temperature superconductivity in lanthanide/actinide extreme superhydrides, J. Am. Chem. Soc. **144**, 13394 (2022).

[27] W. E. Pickett, Room temperature superconductivity: The roles of theory and materials design, Rev. Mod. Phys. **95**, 021001 (2023).

[28] R. J. Hemley, H. K. Mao, G. Shen, J. Badro, P. Gillet, M. Hanfland, and D. Häusermann, X-ray imaging of stress and strain of diamond, iron, and tungsten at megabar pressures, Science **276**, 1242 (1997).

[29] B. Li, C. Ji, W. G. Yang, J. Y. Wang, K. Yang, R. Q. Xu, W. J. Liu, Z. H. Cai, J. H. Chen, and H. K. Mao, Diamond anvil cell behavior up to 4 Mbar, Proc. Natl. Acad. Sci. USA **115**, 1713 (2018).

[30] V. I. Levitas, M. Kamrani, and B. Feng, Tensorial stress-strain fields and large elastoplasticity as well as friction in diamond anvil cell up to 400 GPa, npj Comput. Mater. **5**, 94 (2019).

[31] G. Kresse and J. Furthmüller, Efficiency of ab-initio total energy calculations for metals and semiconductors using a plane-wave basis set, Comput. Mater. Sci. **6**, 15 (1996).

[32] G. Kresse and J. Furthmüller, Efficient iterative schemes for ab initio total-energy calculations using a plane-wave basis set, Phys. Rev. B **54**, 11169 (1996).

[33] J. P. Perdew, K. Burke, and M. Ernzerhof, Generalized gradient approximation made simple, Phys. Rev. Lett. **77**, 3865 (1996).

[34] G. Kresse and J. Joubert, From ultrasoft pseudopotentials to the projector augmented-wave method, Phys. Rev. B **59**, 1758 (1999).

[35] H. J. Monkhorst and J. D. Pack, Special points for Brillouin-zone integrations, Phys. Rev. B **13**, 5188 (1976).

[36] Y. Zhang, H. Sun, and C. Chen, Superhard cubic BC_2N compared to diamond, Phys. Rev. Lett. **93**, 195504 (2004).

[37] Y. Zhang, H. Sun, and C. Chen, Atomistic deformation modes in strong covalent solids, Phys. Rev. Lett. **94**, 145505 (2005).

[38] Z. Pan, H. Sun, and C. Chen, Colossal shear-strength enhancement of low-density cubic BC_2N by nanoindentation, Phys. Rev. Lett. **98**, 135505 (2007).

[39] Z. Pan, H. Sun, Y. Zhang, and C. Chen, Harder than diamond: Superior indentation strength of wurtzite BN and lonsdaleite, Phys. Rev. Lett. **102**, 055503 (2009).

[40] B. Li, H. Sun, and C. Chen, Large indentation strain-stiffening in nanotwinned cubic boron nitride, Nature Commun. **5**, 4965 (2014).

[41] B. Li, H. Sun, and C. Chen, Extreme mechanics of probing the ultimate strength of nanotwinned diamond, Phys. Rev. Lett. **117**, 116103 (2016).

[42] C. Lu, Q. Li, Y. Ma, and C. Chen, Extraordinary indentation strain stiffening produces superhard tungsten nitrides, Phys. Rev. Lett. **119**, 115503 (2017).

[43] C. Liu, X. Gu, K. Zhang, W. Zheng, Y. Ma, and C. Chen, Superhard metallic compound TaB_2 via crystal orientation resolved strain stiffening, Phys. Rev. B **105**, 024105 (2022).

[44] C. Liu, X. Gao, K. Zhang, W. Zheng, and C. Chen, Exceptional strain strengthening and tuning of mechanical properties of TiN, Phys. Rev. B **106**, 054112 (2022).

[45] P. Giannozzi, S. Baroni, N. Bonini, M. Calandra, R. Car, C. Cavazzoni, D. Ceresoli, G. L. Chiarotti, M. Cococcioni, I. Dabo, A. D. Corso, S. d. Gironcoli, S. Fabris, G. Fratesi, R. Gebauer, U. Gerstmann, C. Gougoussis, A. Kokalj, M. Lazzeri, L. Martin-Samos, N. Marzari *et al.*, QUANTUM ESPRESSO: a modular and open-source software project for quantum simulations of materials, J. Phys.: Condens. Matter **21**, 395502 (2009).

[46] S. Baroni, S. de Gironcoli, A. D. Corso, and P. Giannozzi, Phonons and related crystal properties from density-functional perturbation theory, Rev. Mod. Phys. **73**, 515 (2001).

[47] J. Bardeen, L. N. Cooper, and J. R. Schrieffer, Microscopic theory of superconductivity, Phys. Rev. **106**, 162 (1957).

[48] J. Bardeen, L. N. Cooper, and J. R. Schrieffer, Theory of superconductivity, Phys. Rev. **108**, 1175 (1957).

[49] A. B. Migdal, Interaction between electrons and lattice vibrations in a normal metal, Sov. Phys. JETP **7**, 996 (1958).

[50] G. Eliashberg, Interactions between electrons and lattice vibrations in a superconductor, Sov. Phys. JETP **11**, 696 (1960).

[51] See Supplemental Material at http://link.aps.org/supplemental/10.1103/PhysRevB.109.064513 for supporting information on phonon dispersion curves, Eliashberg spectral functions, electron-phonon coupling, electronic band structures, variations of bond lengths, and other physical properties under compressive strains, as well as superconducting properties of YH6 under various biaxial strains combining compression and shear deformation modes.

[52] C. Heil, S. di Cataldo, G. B. Bachelet, and L. Boeri, Superconductivity in sodalite-like yttrium hydride clathrates, Phys. Rev. B **99**, 220502(R) (2019).

[53] H. Wang, Y. Yao, F. Peng, H. Liu, and R. J. Hemley, Quantum and classical diffusion in superconducting clathrate hydrides, Phys. Rev. Lett. **126**, 117002 (2021).

[54] H. Wang, P. T. Salzbrenner, I. Errea, F. Peng, Z. Lu, H. Liu, L. Zhu, C. J. Pickard, and Y. Yao, Quantum structural fluxion in superconducting lanthanum polyhydride, Nature Commun. **14**, 1674 (2023).